

Experimental and modelling study of the recombination reaction $\text{H} + \text{O}_2 (+\text{M}) \rightarrow \text{HO}_2 (+\text{M})$ between 300 and 900 K, 1.5 and 950 bar, and in the bath gases $\text{M} = \text{He}, \text{Ar},$ and N_2

R. X. Fernandes,[†] K. Luther, J. Troe* and V. G. Ushakov[‡]

Received 18th March 2008, Accepted 25th April 2008

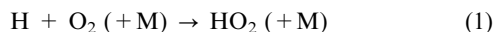
First published as an Advance Article on the web 11th June 2008

DOI: 10.1039/b804553d

The recombination reaction $\text{H} + \text{O}_2 (+\text{M}) \rightarrow \text{HO}_2 (+\text{M})$ was studied by laser flash photolysis in a high pressure flow cell, over the temperature range 300–900 K, the pressure range 1.5–950 bar and in the bath gases $\text{M} = \text{He}$ and N_2 . Earlier experiments by Hahn *et al.* (*Phys. Chem. Chem. Phys.* 2004, **6**, 1997) in the bath gas $\text{M} = \text{Ar}$ were also extended. The data were analyzed in terms of unimolecular rate theory employing new calculations of relevant molecular parameters. Improved energy transfer parameters for the bath gases $\text{M} = \text{He}, \text{Ar}, \text{N}_2$, and H_2O could thus be obtained and complete falloff curves were constructed. In the case of water, the high pressure rates well connect with pulse radiolysis results obtained in supercritical water by Janik *et al.* (*J. Phys. Chem. A* 2007, **111**, 79).

I. Introduction

The recombination reaction



continues to attract considerable attention both on the experimental and on the theoretical side. The low pressure pseudo-second order rate coefficients $k_{1,0}$ are now fairly well established experimentally (see, *e.g.*, ref. 1–7) over a wide temperature range and for a variety of bath gases M . Progress in the understanding of details of the HO_2 potential energy surface,^{8–16} on the other hand, allows for a better theoretical modelling of several of the factors¹⁷ contributing to $k_{1,0}$. Nevertheless, collisional energy transfer parameters remain to be fitted quantities.

The experimental information on the high pressure second order rate coefficient $k_{1,\infty}$ is, by far, less complete. Early experiments from our laboratory¹⁸ up to 200 bar in the bath gases Ar and N_2 (and up to 10 bar in CH_4) at 300 K were limited to the lower half of the falloff curves. More recently¹⁹ we were able to extend the pressure range up to 900 bar and to derive $k_{1,\infty}$ by extrapolation. Temperatures up to 700 K were studied using Ar as the bath gas. Combining these data with classical trajectory calculations on an *ab initio* potential energy surface,⁹ full falloff curves could be constructed which also allowed for an extrapolation to temperatures outside the indicated range. However, the results were limited to the bath gas Ar .

Because of its relevance for high pressure combustion,^{20–22} it appears of interest to have full falloff curves also for other bath gases, in particular, for N_2 . One might also try to see the bath gas influence on the shape of the falloff curves. For this reason, in the present work we have extended the measurements in Ar from ref. 19, included the bath gases N_2 and He , and covered temperatures up to 900 K and pressures up to 950 bar. Besides these experiments, we improved the theoretical modelling in several ways. Anharmonicity and rotational contributions to $k_{1,0}$ and to the falloff curves can be characterized much better now than before, because the relevant input from *ab initio* potentials is now available.^{15,16} This analysis allows one to extract the product of the collision frequency Z and the collision efficiency β_c , and from this the average energy $\langle \Delta E \rangle$ transferred per collision between M and excited HO_2 , with much better precision than possible before. We extend this analysis to the bath gas H_2O for which $k_{1,0}$ is particularly large.^{4,23–25} For this bath gas, we provide a calculation of Z for H_2O – HO_2 collisions from the dipole–dipole capture theory and compare this with earlier results from flexible transition state theoretical (FTST) calculations of Z described in ref. 4 and 6. On this basis, on the one hand, we extract a better value for $\langle \Delta E \rangle$ for H_2O – HO_2 collisions. On the other hand, falloff curves for $\text{M} = \text{H}_2\text{O}$ can be constructed which provide a link to supercritical water conditions. For the latter, the experimental values of $k_{1,\infty}$ were already shown²⁶ to be fully consistent with the results from the classical trajectory calculations of ref. 9.

2. Experimental technique

The reaction of H atoms with molecular oxygen was followed by the detection of the UV absorption of HO_2 at $\lambda = 230$ nm. H atoms were produced by laser flash photolysis of ammonia at 193.3 nm. Our experiments employed the high pressure flow cell²⁷ depicted in Fig. 1. It was made of stainless steel (Inconel

Institut für Physikalische Chemie, Universität Göttingen, Tammannstrasse 6, D-37077 Göttingen, Germany.
E-mail: shoff@gwdg.de

[†] Present address: Combustion Research Facility, Sandia National Laboratories, Livermore, CA 94551-0969, USA.

[‡] Present address: Institute of Problems of Chemical Physics, Russian Academy of Sciences, 142432 Chernogolovka, Russia.

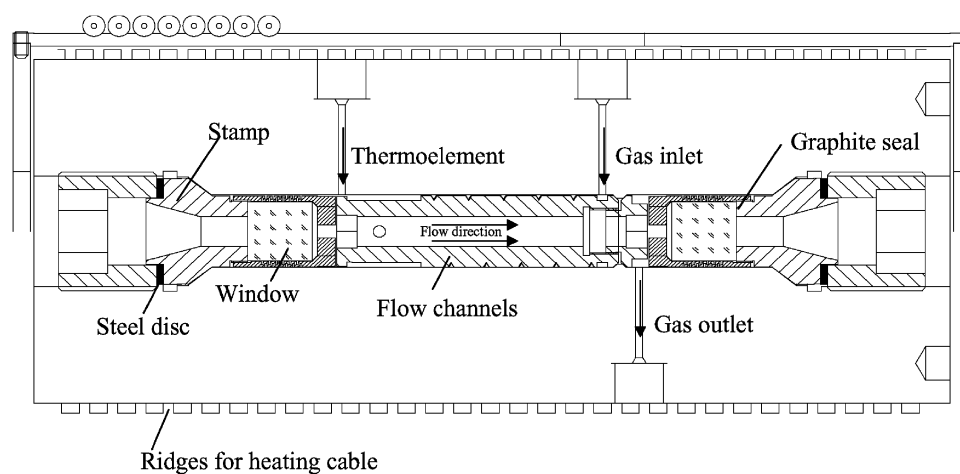


Fig. 1 High pressure flow cell (for a detailed description, see text and ref. 27).

alloy 718, Special Metals) and had an internal diameter of 2.2 cm and an optical path length of 10 cm. Quartz windows with a thickness of 2 cm and diameter of 1.8 cm provided optical access to the cell. The cylindrical reactor possessed an outer diameter of 11 cm with a total length of 26.2 cm. The cell body was surrounded by heating cables. The cell body also contained flow channels such that the reaction mixtures were preheated before finally entering the cell volume. This is illustrated symbolically in Fig. 1 where, from the gas inlet at the right hand side of the cell, the reaction mixture through flow channels in the cell volume is guided to the left hand side of the cell. It then enters the cell through a number of holes surrounding the entrance window, flows through the cell from left to right, and leaves the cell through a number of holes surrounding the exit window and finally enters the gas outlet. The windows are held in position by steel screws, steel discs, steel stamps and graphite seals. The flow rates (up to several tens of litres per minute) were controlled by flow-controllers. The reactor was designed in such a way that complete flushing of the quartz windows was guaranteed. Sufficiently large flow rates were maintained to ensure that the complete cell volume was exchanged before the next laser pulse arrived. For pressures above 100 bar, an oil-free membrane compressor was employed. The temperature could be varied from 300 to 1000 K and measured using Ni–Cr–Ni thermocouples placed both at the inlet and the outlet of the cell. To reduce radiative heat losses, the cell was thermally isolated from the outer surroundings by a reflection mantle of brass, coated with 2 μm of gold to achieve a higher degree of reflection. Two additional gold-coated brass discs surrounded the lateral sides of the cell.

The photolysis and probe light beams were directed in opposite directions along the center through the cell. The photolysis light was provided by an ArF excimer laser (Lambda Physik LPX 130i, 20 ns pulses, 193 nm, up to 100 mJ cm⁻²). The probe light was the collimated output from a 200 W high pressure Xe–Hg lamp (USHIO UXM-200 H). This beam was directed through the cell, dispersed by a monochromator (ZEISS MM 3d) and finally detected by a photomultiplier (RCA 1P28). Cuvettes containing 0.05 molar NaCl solution were placed in the front of the lamp and of the monochromator in order to block out laser light and thereby prevent

interference of the laser pulse with the detection system. The signals were recorded and averaged over about 1000 shots for each experimental point. Furthermore, blank signals with pure nitrogen were recorded under similar conditions as in the experiment. Blank experiments preceded and followed each individual measurement. The optical path, from the photolysis laser to the cell and to the detection system, was continuously flushed with nitrogen.

Reaction mixtures were prepared before the experiments, containing 0.2–100 ppm of NH₃ (Merck, 99.96%), 0.01–1.6% of O₂ (Messer-Griesheim, 99.998%), and the respective bath gases Ar (99.9999%), He (99.999%), and N₂ (99.9995%). The mixtures were kept in stainless steel cylinders with volumes of 50 litres. The cylinders with the reaction mixture were rolled over more than 12 h in order to ensure complete and homogeneous mixing. The mixtures flowed continuously through the cell at the flow rate required to exchange the complete cell volume before each laser pulse. The photolysis of ammonia at 193.3 nm generated H atoms in the reaction mixture which then reacted with oxygen to produce HO₂ radicals. The latter were monitored at 230 nm and the concentrations were calibrated with the absorption coefficients from ref. 28. The temperature dependences of the absorption coefficients are known.²⁹ We found no evidence for major pressure dependences in the bath gases He, Ar, and N₂. On the other hand, marked solvent shifts of the HO₂ spectrum have been observed with polar solvents.³⁰ As HO₂ formation was studied under nearly pseudo-first order conditions, minor uncertainties of the absorption coefficients would not have been a problem.

3. Experimental results

A typical absorption–time profile of HO₂ is shown in Fig. 2. The rise of the signal within about 1 μs could well be separated from the decay taking much longer than 20 μs . The formation of HO₂ was well represented by pseudo-first order time law

$$[\text{HO}_2] = [\text{HO}_2]_{\text{max}} \{1 - \exp(-kt)\} \quad (2)$$

with $k = k_1[\text{O}_2]$. The proportionality of k and $[\text{O}_2]$ was verified over a large range of oxygen concentrations and a plot illustrating this behaviour is given in Fig. 3. The analysis of

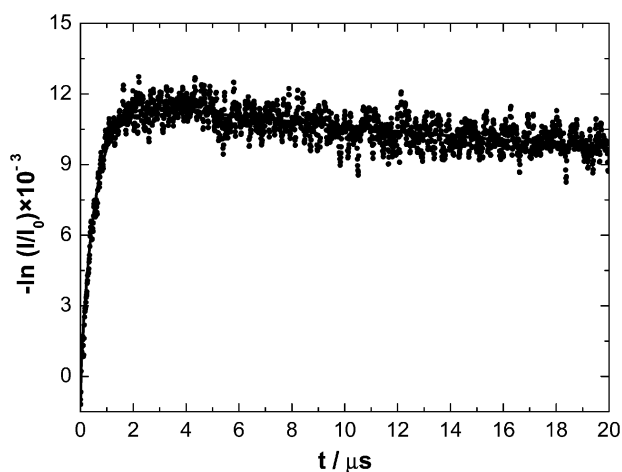


Fig. 2 Absorption-time profile of HO₂ ($\lambda = 230$ nm, $T = 600$ K, $p = 300$ bar, $M = N_2$).

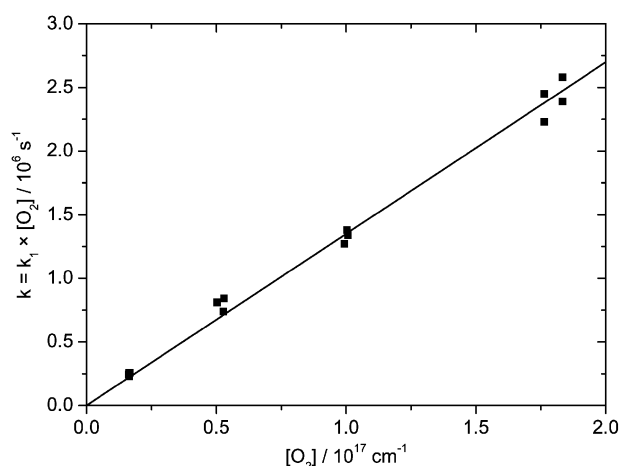


Fig. 3 Dependence of the pseudo-first order rate coefficients $k = k_1[O_2]$ on $[O_2]$ (for $T = 300$ K, $p = 100$ bar, and $M = He$, $k_1 = 1.33(\pm 0.3) \times 10^{-11}$ cm³ molecule⁻¹ s⁻¹).

the absorption-time profiles was facilitated by keeping the absorbance always at values below about 3%. While the rise of the signals was entirely due to reaction (1), at later times the influence of secondary reactions became noticeable. After having determined the values of k_1 from the initial period as represented by eqn (2), the complete absorption-time profiles were modelled using a more detailed reaction mechanism consisting of 22 reactions. Only five of these reactions were found to be relevant for the HO₂ consumption during our observation times. With these reactions and their rate constants from ref. 1–3, the complete HO₂ absorption-time profiles could be reproduced satisfactorily. The dominant reaction responsible for HO₂ consumption was found to be the self-recombination of HO₂. Other reactions of relevance were the self-recombination of NH₂, the reaction of HO₂ with NH₂, and the reactions of H atoms with HO₂ and NH₂. Since the aim of our work was the determination of k_1 , our modelling times were restricted to 20 μ s and HO₂-consuming reactions were not further analyzed. Absorption cross-sections of other species than HO₂, such as NH₃, H₂O₂, N₂H₄, and O₂,

Table 1 Rate coefficients for $H + O_2 (+He) \rightarrow HO_2 (+He)$

T/K	p/bar	$[He]/\text{molecule cm}^{-3}$	$k_1/\text{cm}^3 \text{ molecule}^{-1} \text{ s}^{-1}$
300	1.5	3.6×10^{19}	4.9×10^{-13}
	2.8	6.8×10^{19}	7.8×10^{-13}
	3.0	7.2×10^{19}	8.3×10^{-13}
	10	2.4×10^{20}	2.6×10^{-12}
	30	7.2×10^{20}	6.3×10^{-12}
	100	2.3×10^{21}	1.4×10^{-11}
	300	6.4×10^{21}	3.3×10^{-11}
	900	1.6×10^{22}	4.8×10^{-11}
400	3.8	6.9×10^{19}	8.1×10^{-13}
	10	1.8×10^{20}	1.7×10^{-12}
	30	5.4×10^{20}	4.6×10^{-12}
	100	1.8×10^{21}	1.0×10^{-11}
	300	4.9×10^{21}	2.2×10^{-11}
	900	1.3×10^{22}	3.6×10^{-11}
500	5	7.2×10^{19}	7.1×10^{-13}
	10	1.4×10^{20}	1.1×10^{-12}
	30	4.3×10^{20}	3.4×10^{-12}
	100	1.4×10^{21}	8.0×10^{-12}
	300	4.0×10^{21}	1.7×10^{-11}
	900	1.1×10^{22}	2.8×10^{-11}
600	300	3.4×10^{21}	1.2×10^{-11}
700	300	2.9×10^{21}	9.7×10^{-12}
	900	8.0×10^{21}	1.9×10^{-11}

were also controlled for the analysis wavelength of 230 nm. No perturbation of the HO₂ signals was found.

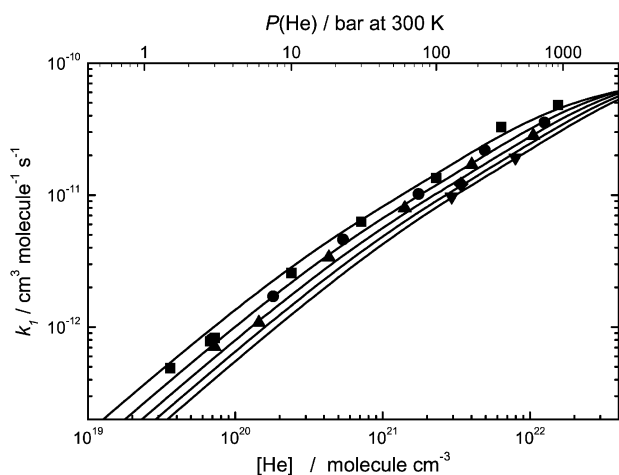
The rate coefficients k_1 derived for the bath gases He, Ar, and N₂ are summarized in Tables 1–3. The pressure dependence of k_1 , observed at fixed temperature, indicates that the reaction was studied in the falloff range of the recombination reaction. Falloff curves were plotted for the entire temperature range investigated experimentally. Fig. 4–6 show such falloff curves for the bath gases He, Ar, and N₂, respectively. One notices that even at pressures of the order of 1000 bar, the

Table 2 Rate coefficients for $H + O_2 (+Ar) \rightarrow HO_2 (+Ar)$

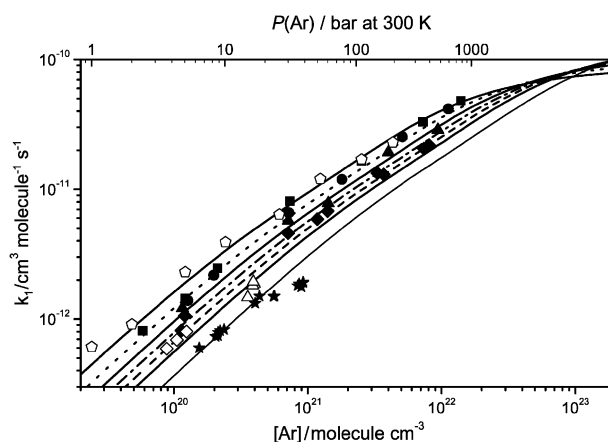
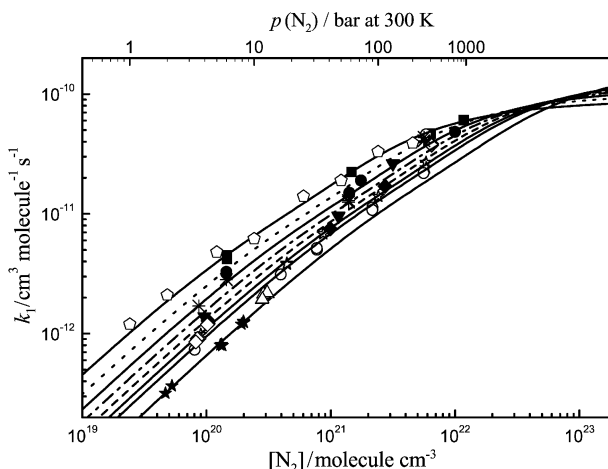
T/K	p/bar	$[Ar]/\text{molecule cm}^{-3}$	$k_1/\text{cm}^3 \text{ molecule}^{-1} \text{ s}^{-1}$
300	2.4	5.8×10^{19}	8.1×10^{-13}
	5.0	1.2×10^{20}	1.4×10^{-12}
	8.7	2.1×10^{20}	2.5×10^{-12}
	30	7.4×10^{20}	8.1×10^{-12}
	100	2.5×10^{21}	1.7×10^{-11}
	300	7.3×10^{21}	3.3×10^{-11}
400	900	1.4×10^{22}	4.8×10^{-11}
	7.0	1.3×10^{20}	1.4×10^{-12}
	11	2.0×10^{20}	2.2×10^{-12}
	40	7.2×10^{20}	6.6×10^{-12}
	100	1.8×10^{21}	1.2×10^{-11}
	300	5.1×10^{21}	2.5×10^{-11}
500	900	1.1×10^{22}	4.2×10^{-11}
	8	1.2×10^{20}	1.2×10^{-12}
	50	7.2×10^{20}	5.7×10^{-12}
	100	1.4×10^{21}	7.8×10^{-12}
	300	4.0×10^{21}	1.9×10^{-11}
	900	9.4×10^{21}	2.9×10^{-11}
600	10	1.2×10^{20}	1.1×10^{-12}
	60	7.1×10^{20}	4.6×10^{-12}
	100	1.2×10^{21}	5.9×10^{-12}
	120	1.4×10^{21}	6.8×10^{-12}
	300	3.3×10^{21}	1.3×10^{-11}
	900	8.1×10^{21}	2.2×10^{-11}
700	11	1.1×10^{20}	8.2×10^{-13}
	400	3.7×10^{21}	1.3×10^{-11}
	950	7.4×10^{21}	2.1×10^{-11}

Table 3 Rate coefficients for $\text{H} + \text{O}_2 (+\text{N}_2) \rightarrow \text{HO}_2 (+\text{N}_2)$

T/K	p/bar	$[\text{N}_2]/\text{molecule cm}^{-3}$	$k_1/\text{cm}^3 \text{ molecule}^{-1} \text{ s}^{-1}$
300	6	1.5×10^{20}	3.9×10^{-12}
	60	1.5×10^{21}	2.1×10^{-11}
	300	6.4×10^{21}	4.1×10^{-11}
	900	1.2×10^{22}	5.7×10^{-11}
400	8	1.5×10^{20}	2.8×10^{-12}
	80	1.4×10^{21}	1.5×10^{-11}
	100	1.7×10^{21}	1.9×10^{-11}
	400	5.9×10^{21}	4.5×10^{-11}
	900	9.8×10^{21}	6.1×10^{-11}
	950	1.0×10^{22}	5.6×10^{-11}
500	6	8.7×10^{19}	1.6×10^{-12}
	10	1.4×10^{20}	2.5×10^{-12}
	100	1.4×10^{21}	1.3×10^{-11}
	500	5.6×10^{21}	4.2×10^{-11}
600	8	9.6×10^{19}	1.3×10^{-12}
	100	1.2×10^{21}	9.6×10^{-12}
	300	3.2×10^{21}	2.5×10^{-11}
	10	1.0×10^{20}	1.2×10^{-12}
700	100	9.9×10^{20}	7.2×10^{-12}
	300	2.7×10^{21}	1.9×10^{-11}
	900	6.5×10^{21}	3.8×10^{-11}
	10	9.0×10^{19}	9.8×10^{-13}
800	50	4.4×10^{20}	3.8×10^{-12}
	100	8.7×10^{20}	6.4×10^{-12}
	300	2.4×10^{21}	1.4×10^{-11}
	900	5.8×10^{21}	2.3×10^{-11}
900	10	8.0×10^{19}	7.3×10^{-13}
	50	4.0×10^{20}	3.3×10^{-12}
	100	7.8×10^{20}	5.1×10^{-12}
	300	2.2×10^{21}	1.1×10^{-11}
	900	5.3×10^{21}	1.7×10^{-11}
	950	5.6×10^{21}	2.0×10^{-11}

**Fig. 4** Falloff curves for the recombination $\text{H} + \text{O}_2 (+\text{He}) \rightarrow \text{HO}_2 (+\text{He})$ (representative upper pressure scale for 300 K; $T/\text{K} = 300$ (■), 400 (●), 500 (▲), 600 (◆), and 700 (▼) and the corresponding fitted curves from eqns (3)–(5) from top to bottom, resp.).

limiting high pressure range it not reached completely, but nevertheless approached sufficiently well to allow for an extrapolation towards $k_{1,\infty}$. One also notices that the falloff curves shift with temperature in a way which makes the extrapolation more difficult with increasing temperature. In order to improve the construction of complete falloff curves, we combined the present measurements with the theoretical modelling of $k_{1,\infty}$ from ref. 9 which was done by trajectory

**Fig. 5** Falloff curves for the recombination $\text{H} + \text{O}_2 (+\text{Ar}) \rightarrow \text{HO}_2 (+\text{Ar})$ (representative upper pressure scale for 300 K; $T/\text{K} = 300$ (■), 400 (●), 500 (▲), and 600 (◆) from this work; 300 (◇, ref. 19), 820 (◇, ref. 20), 1200 (★, ref. 22), and 1325 (△, ref. 21); the fitted curves at left from top to bottom are for $T/\text{K} = 300, 400, 500, 600, 700, 820$, and 1200, resp.).**Fig. 6** Falloff curves for the recombination $\text{H} + \text{O}_2 (+\text{N}_2) \rightarrow \text{HO}_2 (+\text{N}_2)$ (representative upper pressure scale for 300 K; $T/\text{K} = 300$ (■), 400 (●), 500 (▲), 600 (◆), 700 (▼), 800 (☆), and 900 (○) from this work; 300 (◇, ref. 18), 850 (◇, ref. 20), 1200 (★, ref. 22), and 1300 (△, ref. 21); the fitted curves from eqns (3)–(5), at left from top to bottom, are for $T/\text{K} = 300, 400, 500, 600, 700, 800, 900$, and 1200, resp.).

calculations on a high precision *ab initio* potential.^{9–11} The experimental and theoretical values are fully consistent and support each other mutually. Covering wide pressure and temperature ranges, the shown falloff curves also allow for clear indication of how far earlier medium pressure experiments such as from ref. 19–22 were away from the limiting low pressure third order range. Fig. 6 illustrates this behaviour for the bath gas N_2 .

The falloff curves from Fig. 4–6 are at first represented by the empirical falloff expressions from ref. 17 and 31. These expressions are used here with asymmetric broadening factors, *i.e.* in the form

$$k_1/k_{1,\infty} = [x/(1+x)]F_{\text{cent}}^{[1+(a+\log x)^2/(N\pm\Delta N)^2]^{-1}} \quad (3)$$

where $x = k_{1,0}/k_{1,\infty}$, $a \approx 0.3$, $N \approx 1.05$, $\Delta N \approx 0.1$. The limiting rate coefficients

$$k_{1,\infty} = 9.5 \times 10^{-11} (T/300 \text{ K})^{+0.44} \text{ cm}^3 \text{ molecule}^{-1} \text{ s}^{-1} \quad (4)$$

$$k_{1,0} = [\text{He}] 1.8 \times 10^{-32} (T/300 \text{ K})^{-1.2} \text{ cm}^6 \text{ molecule}^{-2} \text{ s}^{-1} \quad (5)$$

$$k_{1,0} = [\text{Ar}] 2.2 \times 10^{-32} (T/300 \text{ K})^{-1.12} \text{ cm}^6 \text{ molecule}^{-2} \text{ s}^{-1} \quad (6)$$

$$k_{1,0} = [\text{N}_2] 4.3 \times 10^{-32} (T/300 \text{ K})^{-1.23} \text{ cm}^6 \text{ molecule}^{-2} \text{ s}^{-1} \quad (7)$$

are from ref. 9, (for $k_{1,\infty}$) and ref. 1–4 (for $k_{1,0}$). In addition, $+\Delta N$ is chosen for $(a + \log x) < 0$ and $-\Delta N$ for $(a + \log x) > 0$, while $F_{\text{cent}} \approx 0.5$ is taken independent of the temperature. The theoretical high pressure rate coefficients $k_{1,\infty}$ in ref. 9 over the range 200–5000 K were represented by

$$k_{1,\infty}/\text{cm}^3 \text{ molecule}^{-1} \text{ s}^{-1} = 7.84 \times 10^{-11} (T/300 \text{ K})^{0.56} + 1.79 \times 10^{-11} (T/300 \text{ K})^{-1.7} \quad (8)$$

Over the range 300–900 K, the simpler form of eqn (4) works similarly well. The limiting low pressure rate coefficients $k_{1,0}$ of eqns (5)–(7) from ref. 1–4 were obtained at much lower pressures than studied here such that falloff corrections practically did not have to be applied. The present experiments were not intended to derive precise values of $k_{1,0}$. However, our falloff curves were fully consistent with the results from the literature.

The described measurements of falloff curves for reaction (1) can be represented in an even more unified way than that given by Fig. 4–6. It had already been found for our experiments with the bath gas Ar in ref. 19 that falloff curves at different temperatures within the experimental scatter could be combined into a single doubly-reduced curve of $k_1/k_{1,\infty}$ as a function of the “reduced pressure” $x = k_{1,0}/k_{1,\infty}$. It appears remarkable that all of our measurements, for the three bath gases He, Ar, and N₂, and over the full temperature range 300–900 K, fall on one doubly-reduced falloff curve such as that shown in Fig. 7. There is some scatter of the measurements but the deviations from the “universal falloff curve” do not seem to exceed about $\pm 25\%$. Obviously, it is of interest to see whether theoretically modelled falloff curves fall into this band as well, see below.

4. Theoretical analysis of low pressure rate coefficients

The experimental values for $k_{1,0}$ have been analyzed before, starting with ref. 32 and repeated more recently, *e.g.*, in ref. 4 and 5. In these studies, the factorized form of $k_{1,0}$ from ref. 19 and 32 was chosen, *i.e.*

$$k_{1,0}(\text{M}) = [\text{M}] Z \beta_c f^*/K_c \quad (9)$$

with the equilibrium population f^* of dissociative states of HO₂ expressed by

$$f^* \approx [\rho_{\text{vib},h}(E_0) kT/Q_{\text{vib}}(\text{HO}_2)] F_E F_{\text{anh}} F_{\text{rot}} \exp(-E_0/kT) \quad (10)$$

The equilibrium constant $K_c = ([\text{H}][\text{O}_2]/[\text{HO}_2])_{\text{eq}}$ is represented by

$$K_c = \Pi(Q_{\text{trans},i} Q_{\text{el},i} Q_{\text{rot},i} Q_{\text{vib},i}) \exp(-E_0/kT) \quad (11)$$

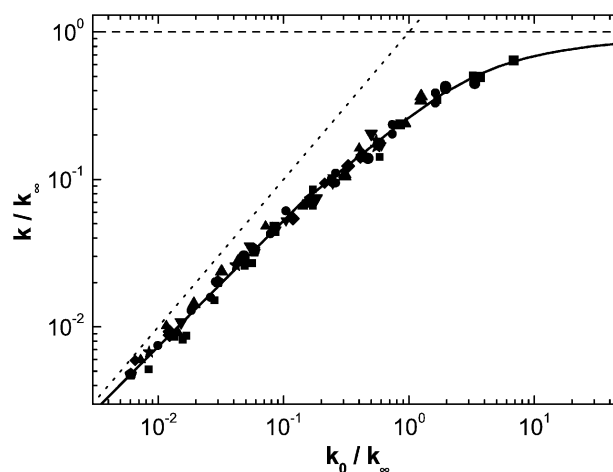


Fig. 7 Doubly reduced falloff curves for the recombination $\text{H} + \text{O}_2 (+\text{M}) \rightarrow \text{HO}_2 (+\text{M})$ in the bath gases $\text{M} = \text{He}, \text{Ar},$ and N_2 (experimental points from this work from Tables 1–3; $T/\text{K} = 300$ (■), 400 (●), 500 (▲), 600 (▼), 700 (◆), 800 (★), and 900 (◆), see text).

with the respective partition functions Q_i (for the meaning of the factors in eqn (10), see ref. 19 and below). Measurements of $k_{1,0}(\text{M})$ provide an access to the product $Z \beta_c$. This quantity unfortunately is still not yet quantitatively available from theory. Therefore, it is important that f^*/K_c is calculated as quantitative as possible such that $Z \beta_c$ and f^*/K_c can be separated. As new *ab initio* information on molecular parameters of HO₂ has become available, the following update of the calculation of f^*/K_c leads to improved experimental values of the product $Z \beta_c$. As a matter of fact, the present analysis is one of the first examples where f^*/K_c is calculated directly for an *ab initio* potential energy surface.

We employ the presently accepted value for the dissociation energy of HO₂ (at 0 K) from the “active thermochemical tables” of ref. 33 which give $E_0 = hc(16785 \pm 20) \text{ cm}^{-1}$. The harmonic vibrational density of states $\rho_{\text{vib},h}(E_0)$ is calculated in Whitten-Rabinovitch form³⁴ with the fundamental frequencies of HO₂ from ref. 35–38. Relative to this value and on the basis of optimized *ab initio* potentials of HO₂, an anharmonicity factor of $F_{\text{anh}}(E_0) = 1.47$ was derived in ref. 15 (it should be noted that, because of the use of fundamentals, $\rho_{\text{vib},h}(E_0)$ already accounts for some anharmonicity; $F_{\text{anh}}(E_0)$ then corresponds to the additional anharmonicity and should be used only together with the given $\rho_{\text{vib},h}(E_0)$). In this way, $\rho_{\text{vib},h}(E_0) = 0.0369/\text{cm}^{-1}$ and $\rho_{\text{vib},h}(E_0) F_{\text{anh}}(E_0) = 0.0544/\text{cm}^{-1}$ are obtained.

The rotational factor $F_{\text{rot}}(E_0)$ requires particular attention. Defined by

$$F_{\text{rot}} = Q_{\text{rot}}^{-1}(\text{HO}_2) \sum_{J=0}^{J_{\text{max}}} (2J+1) \sum_{K=-\min(J, K_{\text{max}})}^{\min(J, K_{\text{max}})} \{ [\rho_{\text{vib},h}(E_0(J)) \times -E_{\text{rot}}(J, K)] / \rho_{\text{vib},h}(E_0(J=0)) \} \times \exp\{-[E_0(J) - E_0(J=0)]/kT\} \quad (12)$$

it depends on the knowledge of the centrifugal barriers $E_0(J) - E_0(J=0)$ (K_{max} denotes the largest K , for which

Table 4 Energy transfer parameters in $\text{H} + \text{O}_2 (+\text{M}) \rightarrow \text{HO}_2 (+\text{M})$ derived from $k_{1,0}$ (M)

	200	300	T/K 500	800	1500	Footnotes
M = He						
Z_{LJ}	3.18	3.56	4.14	4.80	5.92	^a
β_{c}	0.038	0.022	0.013	0.0086	0.0066	^b
$-\langle\Delta E\rangle_{\text{LJ}}$	6.09	5.53	5.10	5.57	8.29	^c
$Z_{\text{id-id}}$	5.73	6.13	6.68	7.22	8.02	^d
β_{c}	0.021	0.013	0.0078	0.0057	0.0049	^b
$-\langle\Delta E\rangle_{\text{id-id}}$	3.49	3.08	3.08	3.63	6.04	^e
M = Ar						
Z_{LJ}	2.59	2.81	3.17	3.60	4.33	^a
β_{c}	0.055	0.034	0.021	0.015	0.013	^b
$-\langle\Delta E\rangle_{\text{LJ}}$	10.2	8.93	8.79	10.2	16.3	^c
$Z_{\text{id-id}}$	4.88	5.22	5.68	6.15	6.83	^d
β_{c}	0.029	0.018	0.012	0.0089	0.0080	^b
$-\langle\Delta E\rangle_{\text{id-id}}$	5.00	4.53	4.71	5.76	10.1	^e
M = N₂						
Z_{LJ}	2.94	3.19	3.60	4.08	4.91	^a
β_{c}	0.100	0.059	0.034	0.023	0.018	^b
$-\langle\Delta E\rangle_{\text{LJ}}$	20.5	16.6	15.0	16.3	24.2	^c
$Z_{\text{id-id}}$	5.49	5.87	6.39	6.92	7.68	^d
β_{c}	0.053	0.032	0.019	0.014	0.012	^b
$-\langle\Delta E\rangle_{\text{id-id}}$	9.79	8.30	8.00	9.23	15.0	^e
M = H₂O						
Z_{LJ}	3.41	3.55	3.85	4.25	4.97	^a
β_{c}	0.86	0.53	0.32	0.23	0.18	^b
$-\langle\Delta E\rangle_{\text{LJ}}$	1670	414	263	252	358	^c
$Z_{\text{d-d}}$	5.76	6.54	7.71	8.96	11.0	^e
β_{c}	0.51	0.29	0.16	0.11	0.081	^b
$-\langle\Delta E\rangle_{\text{d-d}}$	250	132	95	93	131	^c

^a Z_{LJ} in $10^{-10} \text{ cm}^3 \text{ molecule}^{-1} \text{ s}^{-1}$ with ε and σ from ref. 42 and 52. ^b Experimental β_{c} derived from eqns (5)–(7). ^c $-\langle\Delta E\rangle_{\text{LJ}}$ in hc cm^{-1} . ^d $Z_{\text{id-id}}$ in $10^{-10} \text{ cm}^3 \text{ molecule}^{-1} \text{ s}^{-1}$ with ε and σ from ref. 42 and 52 in eqn (15). ^e $Z_{\text{d-d}}$ in $10^{-10} \text{ cm}^3 \text{ molecule}^{-1} \text{ s}^{-1}$ with ε , σ , and μ_{D} from ref. 42 in eqn (16), see also ref. 40).

the rotational energy $E_{\text{rot}}(J, K)$ of the nearly symmetric top obeys $E_{\text{rot}}(J, K) \leq E_0(J)$; J_{max} denotes the largest J for which $E_{\text{rot}}(J, K = 0) \leq E_0(J)$; K is assumed not to be conserved during the lifetime of HO_2^*). The recent classical trajectory and adiabatic channel calculations¹⁵ on the *ab initio* potential of ref. 9 and 10 indicated that the HO_2 system is characterized by transition-state switching which makes earlier estimates of F_{rot} obsolete. There are outer centrifugal barriers in the long-range R^{-6} potential and inner centrifugal barriers near $R \approx 5 a_0$ where R is the $\text{H}-\text{O}_2$ distance ($a_0 = 0.529 \times 10^{-8} \text{ cm}$). This approximately leads to $E_0(J) - E_0(J = 0) \approx 0$ (for $0 \leq J \leq 2$), $\text{hc } 0.06 \text{ cm}^{-1} [J(J + 1)]^{1.5}$ (for $2 < J \leq 15$), and $\text{hc } 0.92 \text{ cm}^{-1} [J(J + 1)]$ (for $J > 15$). The calculation of F_{rot} with these values gives almost the same results as the calculation with the accurate $E_0(J)$. For example, for 300, 800, and 1400 K, the approximate $E_0(J)$ leads to $F_{\text{rot}} = 24.8, 15.1$, and 9.28 , while the accurate $E_0(J)$ gives $F_{\text{rot}} = 25.2, 15.1$, and 9.29 , respectively. The derived values of F_{rot} are substantially larger (a factor of 2–3) than previous estimates^{4,5,32} which were based on oversimplified approximations made in the absence of *ab initio* information on F_{anh} and F_{rot} . This has consequences for the derived $\langle\Delta E\rangle$, see below.

On the basis of the calculated f^*/K_{c} from the *ab initio* potential and the experimental $k_{1,0}(\text{M})$ from eqns (5)–(7), experimental values of the product $Z \beta_{\text{c}}$ are evaluated, see results in Table 4. The table also includes the less certain values for $\text{M} = \text{H}_2\text{O}$ which follow from the experimental

results of

$$k_{1,0}(\text{H}_2\text{O}) \approx ([\text{H}_2\text{O}]/[\text{N}_2]) 10 k_{1,0}(\text{N}_2) \quad (13)$$

from ref. 4,23–25. Mainly because of the changes of F_{rot} , the derived values of the product $Z \beta_{\text{c}}$ are smaller by a factor of 2–3 than the earlier estimates.^{4,5,32} We further analyze the contributions to $Z \beta_{\text{c}}$ in the following, *i.e.*, we consider both the collision frequency Z and the collision efficiency β_{c} . The latter, by analytical solution of the master equation for an exponential collision model,³⁹ are related to the average total energy $\langle\Delta E\rangle$ transferred per collision through

$$\beta_{\text{c}}/(1 - \beta_{\text{c}}^{1/2}) \approx -\langle\Delta E\rangle/F_{\text{E}}kT \quad (14)$$

It is generally assumed that Z can be estimated semiquantitatively such that $\langle\Delta E\rangle$ remains the final fit parameter. However, there is no fundamental reason why the factors $Z \beta_{\text{c}}$ and f^*/K_{c} in eqn (9) should be separable, as the master equation for collisional stabilization of excited HO_2 only contains state-specific rate coefficients $k_{ji} = k(E', J'/E, J)$ for rovibrational collisional energy transfer from state (E, J) to state (E', J') . The appearance of the factor f^*/K_{c} is a consequence of detailed balancing between the k_{ji} and k_{ij} . On the same ground, there is no fundamental reason that the product $Z \beta_{\text{c}}$ should be separable into Z and β_{c} . It is only for practical reasons that this separation is done and that Z is identified with the Lennard-Jones collision frequency Z_{LJ} , see ref. 39. When more detailed knowledge on

the k_{ji} becomes available, this reference collision frequency could be modified. However, for the time being, Z_{LJ} is a convenient reference quantity, relative to which β_c is derived experimentally. Ref. 4 discussed in detail alternative options for Z . In the following, we propose two more options. We emphasize, however, that the given alternatives for Z are no less or more plausible than the collision frequencies used in previous analysis. For collisions with polarizable collision partners M which do not possess permanent dipole moments, we compare Z_{LJ} with induced dipole-induced dipole capture rate constants⁴⁰ Z_{id-id} . For collisions between two polar collision partners, Z_{LJ} obviously is even less appropriate. By analogy to collisions between ions and polarizable M , for which the ion-induced dipole Langevin capture rate constants are generally used,⁴¹ for $\text{HO}_2\text{-H}_2\text{O}$ collisions we employ the dipole-dipole capture rate constants Z_{d-d} from ref. 40. It was suggested in ref. 4 to calculate Z for dipole-dipole collisions by flexible transition state theory (FTST). The present approach appears simpler to use and follows the general concept of determining Z by capture theory. Table 4 gives Z_{LJ} , see ref. 32, the induced dipole-induced dipole capture rate constants Z_{id-id} for the collision pairs $\text{HO}_2\text{-M}$ with $M = \text{He}, \text{Ar}, \text{and } \text{N}_2$, and the dipole-dipole capture rate constants Z_{d-d} for $M = \text{H}_2\text{O}$. Optimized Lennard-Jones parameters ϵ/k and σ , as well as dipole moments are from ref. 42. Following ref. 40, the induced dipole-induced dipole capture rate constant Z_{id-id} is given by

$$Z_{id-id} = \Gamma(2/3) (2C_6)^{1/3} (kT)^{1/6} (8\pi/\mu)^{1/2} \quad (15)$$

with the van der Waals constant $C_6 = 4\epsilon\sigma^6$. Table 4 shows that Z_{LJ} is about a factor of $1.8(\pm 0.1)$ larger than Z_{id-id} . The dipole-dipole capture rate constants Z_{d-d} from ref. 40 include induced dipole-induced dipole and permanent dipole-permanent dipole contributions. They are given by

$$Z_{d-d} = f_{\text{rigid}} \Gamma(1/3) (\mu_{D_1} \mu_{D_2})^{2/3} (kT)^{-1/6} (8\pi/\mu)^{1/2} \quad (16)$$

with the dipole moments μ_{D_1} and μ_{D_2} of HO_2 and H_2O . The rigidity factors f_{rigid} in eqn. (16) depend on the parameter $\theta = C_6 kT (\mu_{D_1} \mu_{D_2})^{-2}$ and are given in analytical form in ref. 40 (see Fig. 2 of ref. 40). Table 4 includes Z_{d-d} . The FTST calculations from ref. 4 gave approximately $Z_{d-d} = 2.2 \times 10^{-9} \text{ cm}^3 \text{ molecule}^{-1} \text{ s}^{-1}$ which is about a factor of 2–3 larger than the present capture rate constants. The reasons for this discrepancy are difficult to trace.

Choosing Z from the options given above, leads to the experimental values of β_c given in Table 4. They are then converted into average total energies transferred per collision $\langle \Delta E \rangle$, such as also included in Table 4, through eqn (14). It should be stressed that β_c and $\langle \Delta E \rangle$ should always be given together with the employed model for Z . It should also be noted that, within the exponential collision model, $\langle \Delta E \rangle$ and $\langle \Delta E_{\text{down}} \rangle$ are approximately related by³⁹

$$\langle \Delta E \rangle \approx -\langle \Delta E_{\text{down}} \rangle [(\langle \Delta E_{\text{down}} \rangle / (\langle \Delta E_{\text{down}} \rangle + F_E kT))] \quad (17)$$

such that $\langle \Delta E \rangle$ and $\langle \Delta E_{\text{down}} \rangle$ have different temperature dependences. The results of Table 4, in agreement with earlier conclusions^{17,32,43–45} within experimental scatter indicate an only weak temperature dependence of $\langle \Delta E \rangle$ which then roughly corresponds to $\langle \Delta E_{\text{down}} \rangle \propto T^{0.5}$. The present experimental values of

$\langle \Delta E \rangle$ may be compared with classical trajectory calculations for energy transfer of excited triatomic molecules.^{46–49} Early trajectory calculations for $\text{HO}_2\text{-He}$ collisions from ref. 47 led to values β_c which were more than one order of magnitude larger than those derived now. More recent work on energy transfer of excited CS_2 led to much better agreement between experiment^{44,45} and theory^{48,49} and resulted in similarly small values of $-\langle \Delta E \rangle$ as derived in the present work. The $\langle \Delta E \rangle$ -values obtained for $M = \text{H}_2\text{O}$ in the present work indicate that even H_2O is not a “strong collider” and β_c is clearly below unity. The given analysis confirms that more work needs to be done in order to arrive at a quantitative understanding of energy transfer.

5. Theoretical analysis of falloff curves

After having fitted $\langle \Delta E \rangle$ -values from the experimental values of $k_{1,0}$ and accepting $k_{1,\infty}$ from the theoretical modelling on the *ab initio* potential of ref. 9, it remains to analyze the reduced falloff curves which interpolate between $k_{1,0}$ and $k_{1,\infty}$. We do this on the basis of the broadening factors

$$F(x) = (k_1/k_{1,\infty}) (1 + x)/x \quad (18)$$

with $x = k_{1,0}/k_{1,\infty}$. The form of $F(x)$ given by eqn (3) was more or less empirical and needs to be validated by theoretical modelling. At first, we consider strong-collision broadening factors (approached by $\beta \rightarrow 1$ and $-\langle \Delta E \rangle / F_E kT \gg 1$). For this case, standard strong collision unimolecular rate theory provides the general formalism, see, e.g., ref. 31. On the basis of the anharmonic rovibrational densities of states $\rho(E, J)$ and the specific rate constants $k(E, J)$ for HO_2 dissociation from the *ab initio* calculations of the potential from ref. 15, the formalism can be elaborated in detail⁵⁰ and cruder earlier falloff expressions can be replaced by more realistic calculations. We have done such strong collision falloff calculations on two levels, either with continuous variation of the rotational quantum number j of O_2 , or with quantized values of j (only odd values, corresponding to the nuclear-spin statistical weights of the rotational levels of $^{16}\text{O}_2$). The particular transition-state switching character of the HO_2 -system¹⁵ leads to some differences between the two reduced falloff curves. Fig. 8 and 9 demonstrate this behaviour. They also show that the temperature dependence of the broadening factors is only small and that the broadening factors are asymmetric.

In order to compare experimental falloff curves with the calculated strong collision falloff curves, the experimental doubly reduced falloff curves of Fig. 7 can be converted into broadening factors. Alternatively, analogous to Fig. 7, one might plot Fig. 9 in doubly reduced form, see Fig. 10. One immediately realizes that the experimental center broadening factors $F_{\text{cent}} \approx 0.5$ are smaller than the calculated strong collision values of $F_{\text{cent}}^{\text{SC}} = 0.75 \pm 0.03$ of Fig. 8 and 9. It is known from solutions of the master equation in the falloff range¹⁷ that weak collisions result in a further broadening of the strong collision falloff curves. To a first approximation, this effect was represented¹⁷ by the dependence of the center broadening factors $F_{\text{cent}} = F_{\text{cent}}^{\text{SC}} F_{\text{cent}}^{\text{WC}}$ on the collision efficiency β_c through a factor

$$F_{\text{cent}}^{\text{WC}} \approx \beta_c^{0.14} \quad (19)$$

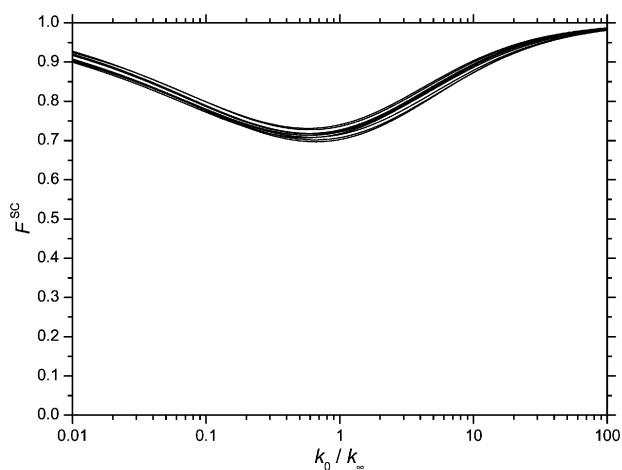


Fig. 8 Modelled strong collision broadening factors F_{sc} for $\text{H} + \text{O}_2 \rightarrow \text{HO}_2$ ($T/\text{K} = 100 \times 20^{(n-1)/9}$ with $n = 1, \dots, 10$ from top to bottom at $k_0/k_\infty = 1$; continuous rotational quantum numbers j of O_2 , see text).

With $\beta_c = 0.022, 0.034, 0.059$, and 0.29 , this would give $F_{cent}^{wc} \approx 0.59, 0.62, 0.67$, and 0.84 at 300 K for $\text{M} = \text{He}, \text{Ar}, \text{N}_2$, and H_2O , respectively. The values of F_{cent}^{wc} roughly make up for the difference between the experimental $F_{cent} \approx 0.5$ and the calculated $F_{cent}^{sc} \approx 0.75$ (for $\text{M} = \text{H}_2\text{O}$ no experimental falloff curves are available). The predicted decrease of F_{cent} with increasing temperature due to the decrease of F_{cent}^{wc} appears to be too small to be visible within the experimental scatter of Fig. 7. At this stage, therefore, it does not appear reasonable to lead the analysis of the experimental data for $\text{M} = \text{He}, \text{Ar}$, and N_2 beyond this point, because eqn (3) gives a good representation of all experimental data and, within the experimental scatter, appears to be consistent with the theoretical calculations. In particular, the asymmetric form of the broadening factor of eqn (3) is supported by the modelling.

The present modelling also allows one to predict falloff curves for $\text{M} = \text{H}_2\text{O}$ which so far have not been measured. Because of the larger value of β_c , F_{cent} is estimated to be close

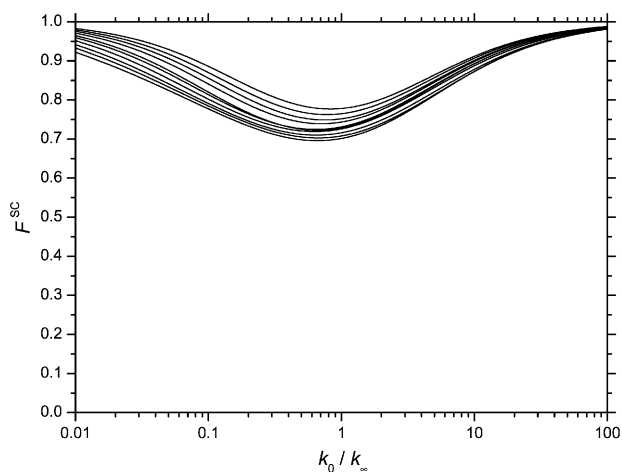


Fig. 9 Modelled strong collision broadening factors F_{sc} for $\text{H} + \text{O}_2 \rightarrow \text{HO}_2$ ($T/\text{K} = 100 \times 20^{(n-1)/9}$ with $n = 1, \dots, 10$ from top to bottom at $k_0/k_\infty = 1$; quantized rotational quantum numbers j of O_2 , odd j only, see text).

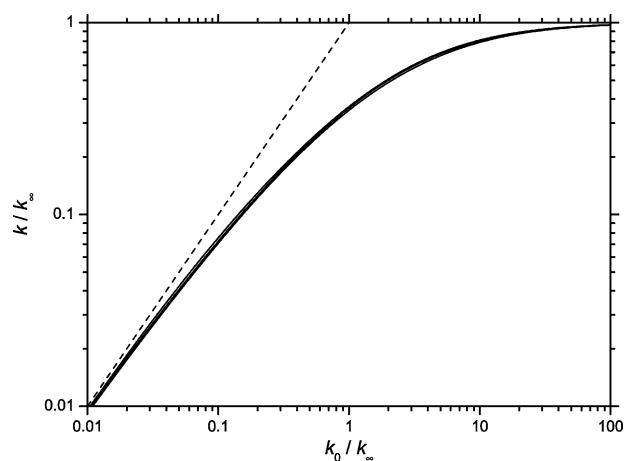


Fig. 10 Modelled strong collision falloff curves for $\text{H} + \text{O}_2 \rightarrow \text{HO}_2$ (results from Fig. 9 for $T/\text{K} = 300, 800$, and 1500 K from top to bottom, see text).

to 0.6 . One further deduces that, at the density of liquid water, reaction (1) is indeed near to the high pressure limit. In this case, the comparison of $k_{1,\infty}$ from the extrapolations of this work and from the calculations from ref. 9 with the pulse radiolysis experiments from ref. 26 appears justified and the internal consistency looks convincing.

The present experiments extend up to such high pressures that deviations from ideal gas behaviour have to be taken into account. This applies in particular when falloff curves for $\text{M} = \text{H}_2\text{O}$ are of interest. As we use $x = k_0/k_\infty$ as our reduced pressure scale and as k_0 relates to collisional energy transfer, we may refer to experimental studies of energy transfer in supercritical fluids. It was shown in ref. 51 that collisional energy transfer rates scale with the radial distribution function at Lennard-Jones contact of the collision partners. This would somewhat distort the representation of the experimental points in the upper half of the doubly reduced falloff curve of Fig. 7. It appears, however, to be only of minor importance for the present analysis.

6. Conclusions

The present work provided experimental falloff curves of reaction (1) in the bath gases $\text{M} = \text{He}, \text{Ar}$, and N_2 over wide temperature and pressure ranges. For the bath gas $\text{M} = \text{H}_2\text{O}$, falloff curves became predictable after energy transfer parameters were extracted from experimental low pressure rate coefficients. The analytical representation of the limiting low and high pressure rate coefficients as well as the intermediate falloff curves allows for an extrapolation both to lower and higher temperatures outside the range $300\text{--}900\text{ K}$ studied in our work. Rate coefficients for high pressure combustion and supercritical water oxidation conditions can thus be also estimated reliably.

Note added in proof

After this article was accepted for publication, we learned about a new modelling of the temperature and pressure dependence of the title reaction.⁵³ This modelling led to values

of $k_{1,\infty}$ which were about 25% lower than the results from ref. 9 used in the present work, and to values of $F_{\text{cent}}(\text{Ar}) = 0.72$ and $F_{\text{cent}}(\text{N}_2) = 0.73$ which were about 50% larger than the present $F_{\text{cent}} = 0.5$. While the difference in $k_{1,\infty}$ can be attributed to slightly higher energies of the inner transition state, the differences in F_{cent} are due to a less complete experimental data base used in ref. 53, and to different absolute values and temperature dependences of $\langle \Delta E \rangle$ arising from a less detailed analysis of $k_{1,0}$.

Acknowledgements

The experimental contribution by J. Hahn and L. Krasnoperov reported in ref. 19 is gratefully acknowledged. We are also grateful for financial support of this work by the Deutsche Forschungsgemeinschaft (SFB 357 "Molekulare Mechanismen Unimolekularer Reaktionen").

References

1. R. Atkinson, D. L. Baulch, R. A. Cox, J. N. Crowley, R. F. Hampson, R. G. Hynes, M. E. Jenkins, M. J. Rossi and J. Troe, *Atmos. Chem. Phys.*, 2004, **4**, 1461.
2. S. P. Sander, R. R. Friedl, D. M. Golden, M. J. Kurylo, R. E. Huie, V. L. Orkin, G. K. Moortgat, A. R. Ravishankara, C. E. Kolb, M. J. Molina and B. J. Finlayson-Pitts, *JPL Publ.* 02-25, 2003(NASA-JPL, 2003).
3. D. L. Baulch, C. T. Bowman, C. J. Cobos, R. A. Cox, Th. Just, J. A. Kerr, M. J. Pilling, K. Stocker, J. Troe, W. Tsang, R. W. Walker and J. Warnatz, *J. Phys. Chem. Ref. Data*, 2005, **34**, 757.
4. J. V. Michael, M.-C. Su, J. W. Sutherland, J. J. Carroll and A. F. Wagner, *J. Phys. Chem. A*, 2002, **106**, 5297.
5. J. Troe, *Proc. Combust. Inst.*, 2000, **28**, 1463.
6. A. F. Wagner, *Proc. Combust. Inst.*, 2002, **29**, 1173.
7. J. A. Miller, M. J. Pilling and J. Troe, *Proc. Combust. Inst.*, 2005, **30**, 43.
8. M. R. Pastrana, L. A. M. Quintales, J. Brandão and A. J. C. Varandas, *J. Phys. Chem.*, 1990, **94**, 8073; M. R. Pastrana, L. A. M. Quintales, J. Brandão and A. J. C. Varandas, *J. Chem. Phys.*, 1992, **96**, 5137.
9. L. B. Harding, J. Troe and V. G. Ushakov, *Phys. Chem. Chem. Phys.*, 2000, **2**, 631.
10. C. Xu, D. Xie, D. H. Zhang, S. Y. Lin and H. Guo, *J. Chem. Phys.*, 2005, **122**, 244305.
11. C. Xu, B. Jiang, D. Xie, S. C. Farantos, S. Y. Lin and H. Guo, *J. Phys. Chem. A*, 2007, **111**, 10353.
12. A. Dobbyn, M. Stumpf, H.-M. Keller and R. Schinke, *J. Chem. Phys.*, 1996, **104**, 8357.
13. V. A. Mandelshtam, T. P. Grodzanov and H. S. Taylor, *J. Chem. Phys.*, 1995, **103**, 10074.
14. H. Zhang and S. C. Smith, *J. Chem. Phys.*, 2002, **116**, 2354; H. Zhang and S. C. Smith, *J. Chem. Phys.*, 2002, **117**, 5174; H. Zhang and S. C. Smith, *J. Chem. Phys.*, 2003, **118**, 10042.
15. J. Troe and V. G. Ushakov, *J. Chem. Phys.*, 2008, **128**, 204307.
16. J. Troe and V. G. Ushakov, *Chem. Phys.*, 2008, **346**, 186; J. Troe and V. G. Ushakov, *Chem. Phys.*, 2008, **346**, 193.
17. J. Troe, *J. Phys. Chem.*, 1979, **83**, 114.
18. C. J. Cobos, H. Hippler and J. Troe, *J. Phys. Chem.*, 1985, **89**, 342.
19. J. Hahn, L. Krasnoperov, K. Luther and J. Troe, *Phys. Chem. Chem. Phys.*, 2004, **6**, 1997.
20. M. A. Mueller, R. A. Yetter and F. L. Dryer, *Proc. Combust. Inst.*, 1998, **27**, 177.
21. D. F. Davidson, E. L. Petersen, M. Roehrig, R. K. Hanson and C. T. Bowman, *Proc. Combust. Inst.*, 1996, **26**, 481.
22. R. W. Bates, D. M. Golden, R. K. Hanson and C. T. Bowman, *Phys. Chem. Chem. Phys.*, 2001, **3**, 2337.
23. K.-J. Hsu, S. M. Anderson, J. L. Durant and F. Kaufman, *J. Phys. Chem.*, 1989, **93**, 1018.
24. K. L. Carleton, W. J. Kessler and W. J. Marinelli, *J. Phys. Chem.*, 1993, **97**, 6412.
25. P. J. Ashman and B. S. Haynes, *Proc. Combust. Inst.*, 1998, **27**, 195.
26. I. Janik, D. M. Bartels, T. Marin and C. Jonah, *J. Phys. Chem. A*, 2007, **111**, 79.
27. R. X. Fernandes, K. Luther and J. Troe, *J. Phys. Chem. A*, 2006, **10**, 4442.
28. P. D. Lightfoot and A. A. Jemi-Alade, *J. Photochem. Photobiol., A*, 1991, **59**, 1.
29. H. Kijewski and J. Troe, *Helv. Chim. Acta*, 1972, **55**, 205.
30. G. Czapski and L. M. Dorfman, *J. Phys. Chem.*, 1964, **68**, 1169.
31. J. Troe, *Ber. Bunsen-Ges. Phys. Chem.*, 1983, **87**, 161; R. G. Gilbert, K. Luther and J. Troe, *Ber. Bunsen-Ges. Phys. Chem.*, 1983, **87**, 169.
32. J. Troe, *J. Chem. Phys.*, 1977, **66**, 4758.
33. B. Ruscic, R. E. Pinzon, M. L. Morton, N. K. Srinivasan, M.-C. Su, J. W. Sutherland and J. V. Michael, *J. Phys. Chem. A*, 2006, **110**, 6592.
34. G. Z. Whitten and B. S. Rabinovitch, *J. Chem. Phys.*, 1963, **38**, 2466.
35. C. Yamada, Y. Endo and E. Hirota, *J. Mol. Spectrosc.*, 1981, **89**, 520.
36. K. Nagai, Y. Endo and E. Hirota, *J. Mol. Spectrosc.*, 1981, **89**, 520.
37. J. B. Burkholder, P. D. Hammer, C. J. Howard, J. P. Towle and J. M. Brown, *J. Mol. Spectrosc.*, 1992, **151**, 493.
38. D. D. Nelson and M. S. Zahniser, *J. Mol. Spectrosc.*, 1991, **150**, 527.
39. J. Troe, *J. Chem. Phys.*, 1977, **66**, 4745.
40. A. I. Maergoiz, E. E. Nikitin, J. Troe and V. G. Ushakov, *J. Chem. Phys.*, 1996, **105**, 6277.
41. A. I. Fernandez, A. A. Viggiano, T. M. Miller, S. Williams, I. Dotan, J. V. Seeley and J. Troe, *J. Phys. Chem. A*, 2004, **108**, 9652.
42. P. Paul and J. Warnatz, *Proc. Combust. Inst.*, 1998, **27**, 495.
43. H. Endo, K. Glänzer and J. Troe, *J. Phys. Chem.*, 1979, **83**, 2083.
44. J. E. Dove, H. Hippler, H. J. Plach and J. Troe, *J. Chem. Phys.*, 1987, **82**, 1907.
45. M. Heymann, H. Hippler, H. J. Plach and J. Troe, *J. Chem. Phys.*, 1987, **87**, 3867.
46. A. J. Stace and J. N. Murrell, *J. Chem. Phys.*, 1978, **68**, 3028.
47. N. J. Brown and J. A. Miller, *J. Chem. Phys.*, 1984, **80**, 5568.
48. G. Lendvay and G. C. Schatz, *J. Phys. Chem.*, 1988, **92**, 7223; G. Lendvay and G. C. Schatz, *J. Phys. Chem.*, 1991, **95**, 8748; G. Lendvay and G. C. Schatz, *J. Phys. Chem.*, 1992, **96**, 3752.
49. G. Lendvay and G. C. Schatz, *J. Chem. Phys.*, 1992, **96**, 4356.
50. J. Troe and V. G. Ushakov, *Faraday Discuss.*, 2001, **119**, 145.
51. D. Schwarzer, J. Troe and M. Zerezke, *J. Chem. Phys.*, 1997, **107**, 8380.
52. R. C. Reid, J. M. Prausnitz and T. K. Sherwood, *The Properties of Gases and Liquids*, McGraw-Hill, New York, 3rd edn, 1977.
53. S. R. Sellevåg, Y. Georgievskii and J. A. Miller, *J. Phys. Chem. A*, 2008, **112**, , DOI: 10.1021/jp711800z.